Research article

Heng Wang, Kang Du, Ruibin Liu, Xinhai Dai, Wending Zhang, Soo Jin Chua and Ting Mei*

Role of hot electron scattering in epsilon-near-zero optical nonlinearity

https://doi.org/10.1515/nanoph-2020-0266
Received May 3, 2020; accepted July 9, 2020; published online July 25, 2020

Abstract: The physical origin of epsilon-near-zero (ENZ) optical nonlinearity lies in the hot-electron dynamics, in which electron scattering plays an important role. With the damping factor defined by hot electron scattering time, the Drude model could be extended to modeling ENZ optical nonlinearity completely. We proposed a statistical electron scattering model that takes into account the effect of electron distribution in a nonparabolic band and conducted the investigation on indium tin oxide (ITO) with femtosecond-pump continuum-probe experiment. We found that ionized impurity scattering and acoustic phonon scattering are the two major scattering mechanisms, of which the latter had been neglected before. They dominate at low-energy and high-energy electrons, respectively, and are weakened or boosted for high electron temperature, respectively. The electron energy–dependent scattering time contributed from multiple scattering mechanisms shows the electron density–dependent damping factor. The comprehensive understanding of electron scattering in ITO will help to develop a complete model of ENZ optical nonlinearity.

Keywords: electron scattering; epsilon-near-zero; free electron optical nonlinearity; intraband transition.

Large optical nonlinearities of transparent conductive oxides [1, 2] have been found in their epsilon-near-zero (ENZ) wavelengths [3–5]. What makes ENZ special is that the enhancement of the electrical field is inversely proportional to the permittivity and the change in refractive index is inversely proportional to the square root of permittivity [6, 7]. Owing to these two effects, the Kerr-like optical nonlinearity is significantly enhanced [8]. The physical origin of ENZ optical nonlinearities is considered to be the intraband transition–induced changes of hot electron properties, in which the electron temperature could rise up to thousands of Kelvin and electron redistributes in the conduction band [7, 9]. With a redefined electron overall effective mass considering the electron redistribution in the nonparabolic conduction band, the Drude model is extended to partially model the ENZ optical nonlinearity [7]. However, a complete model also needs the knowledge of electron scattering, which defines the damping factor. Besides, electron scattering plays an important role on optical response [10], electrical properties [11, 12], and plasmonic resonance in ENZ materials [13, 14]. Unfortunately, the damping factor is treated as a constant as an approximation in describing the nonlinear optical process [9, 15]. Later, an increase in damping factor caused by intraband pumping has therefore to be taken into account in describing the nonlinear optical process [7, 16] implies that electron scattering mechanisms have to be further understood.

Indium tin oxide (ITO) is the most attractive ENZ material because its ENZ wavelength could be tuned to covering both optical communication bands [17, 18] and its excellent optical and electrical performance [12]. It was

***Corresponding author: Ting Mei**, MOE Key Laboratory of Material Physics and Chemistry Under Extraordinary Conditions, and Shaanxi Key Laboratory of Optical Information Technology, School of Physical Science and Technology, Northwestern Polytechnical University, Xi'an 710129, China, E-mail: ting.mei@ieee.org. https://orcid.org/0000-0001-7756-040X

Heng Wang, Kang Du, Xinhai Dai and Wending Zhang: MOE Key Laboratory of Material Physics and Chemistry Under Extraordinary Conditions, and Shaanxi Key Laboratory of Optical Information Technology, School of Physical Science and Technology, Northwestern Polytechnical University, Xi'an 710129, China. https://orcid.org/0000-0003-3692-0848 (H. Wang). https://orcid.org/0000-0002-2151-9819 (K. Du). https://orcid.org/0000-0003-1411-1425 (W. Zhang)

Ruibin Liu: Department of Physics and Center of Theoretical and Computational Physics, The University of Hong Kong, Pokfulam Road, Hong Kong, China

Soo Jin Chua: MOE Key Laboratory of Material Physics and Chemistry Under Extraordinary Conditions, and Shaanxi Key Laboratory of Optical Information Technology, School of Physical Science and Technology, Northwestern Polytechnical University, Xi'an 710129, China; Department of Electrical and Computer Engineering, National University of Singapore, 4 Engineering Drive 3, Singapore 117583, Singapore; and LEES Program, Singapore-MIT Alliance for Research & Technology (SMART), 1 CREATE Way, #10-01 CREATE Tower, Singapore 138602, Singapore

concluded from the electron density–dependent mobility that the dominant scattering mechanism of ITO was ionized impurity scattering [19–21]. By introducing a wavelength-dependent damping based on the ionized impurity scattering theory, the optical transmittance spectrum calculated from the Drude model fits better to the experimental results [10, 22–24]. However, these investigations were carried out with an electron density lower than $1 \times 10^{21}/\text{cm}^3$ and with the operating temperature range of the samples limited to below the annealing temperature of ITO [25–27]. It is unclear whether the dominant scattering mechanism remains the same at higher electron densities. Besides, the knowledge of electron scattering in ITO may not be sufficient for understanding optical nonlinear process involving hot electrons.

In this article, we propose the multiple scattering mechanisms and establish a statistical electron scattering model to incorporate the effect of electron distribution in a nonparabolic band, and a complete extended Drude model is built for the ENZ Kerr-like optical nonlinearity. Femtosecond-pump continuum-probe measurement is conducted in the investigation of ITO. The nonequilibrium electron distribution created by optical pumping is treated under the quasi-thermal equilibrium approximation in the form of the Fermi-Dirac distribution [9, 16] as the electron-electron scattering is faster than other scattering mechanisms [28–31]. Optical properties are characterized via optical probing, and then, electron scattering times and the electron temperature are extracted from the measured transmittance and reflectance spectra. Based on model fitting results, the contributions of different scattering mechanisms are determined. It is revealed that among the four scattering mechanisms, neutral impurity, optical phonon, ionized impurity, and acoustic phonon, the latter two are found to be the major mechanisms, with the last not previously considered important. Furthermore, it is shown that the contributions of these two mechanisms have opposite dependences on electron temperature and electron density, and neither mechanism can unconditionally dominate electron damping.

The E–k relation of a nonparabolic conduction band (Figure 1a) can be written in the first-order approximation [1, 9].

$$\frac{\hbar^2 k^2}{2m_0^*} = \Gamma(E) = E + CE^2, \tag{1}$$

where $\hbar$ is the reduced Planck constant, k is the electron wave vector, m_0^* is the electron effective mass at the conduction band minimum, E is the electron energy referenced to the conduction band minimum, and C is the first-order nonparabolicity factor (C = 0 for parabolic band). The electron energy–dependent scattering time has the same form [1, 32].

$$\tau_{**}(E) = \tau_{0**}\Gamma^{s/2}\left(\frac{d\Gamma}{dE}\right)^{-1}, \tag{2}$$

where the subscript $**$ represents AP, NI, OP, or II for acoustic phonon, neutral impurity, optical phonon, and ionized impurity electron scattering mechanisms, respectively. The factor τ_{0**}, with a dimension of second·eV$^{-s/2}$, has a more detailed form determined by basic physical parameters for each scattering mechanism [33–35], but is merely dealt with a single parameter for simplicity. The factor s accounts for different scattering mechanisms, i.e., s = –1, 0, 1, and 3 for AP, NI, OP, and II, respectively.

The electron energy–dependent scattering time including contributions from the four scattering mechanisms is written as follows:

$$\frac{1}{\tau(E)} = \frac{1}{\tau_{\text{AP}}(E)} + \frac{1}{\tau_{\text{NI}}(E)} + \frac{1}{\tau_{\text{OP}}(E)} + \frac{1}{\tau_{\text{II}}(E)}, \tag{3}$$

and the electron overall scattering time is then statistically averaged over all conduction electrons as follows:

$$\frac{1}{\langle\tau\rangle} = \frac{\int_0^\infty \frac{1}{\tau(E)} N_D f_0 dE}{N}, \tag{4}$$

where $N_D = \Gamma^{1/2}(d\Gamma/dE)(2m_0^*/\hbar^2)^{3/2}/(2\pi^2)$ is density of states; N is the electron density, as defined by [36];

$$N = \int_0^\infty N_D f_0 \, dE \tag{5}$$

and f_0 is the distribution function. The Fermi-Dirac distribution of conduction electrons should be adopted for a degenerate semiconductor like ITO, i.e., $f_0 = \{\exp[(E - E_F)/(k_B T_e)] + 1\}^{-1}$, where E_F is the Fermi level, T_e is the electron temperature, and k_B is the Boltzmann constant. Similarly, the overall effective mass taking into account the electron distribution is determined as follows [7]:

$$\frac{1}{\langle m^*\rangle} = \frac{\int_0^\infty \frac{1}{m_D^*(E)} N_D f_0 \, dE}{N}, \tag{6}$$

where $m_D^*(E) = m_0^* d\Gamma/dE$ is the density-of-states effective mass.

The electron energy–dependent scattering times of different mechanisms are plotted in Figure 1b for both parabolic and nonparabolic bands, in which τ_{0**} = 1 second · eV$^{-s/2}$ is assumed for normalized comparison. It can be seen that the ionized impurity scattering, which

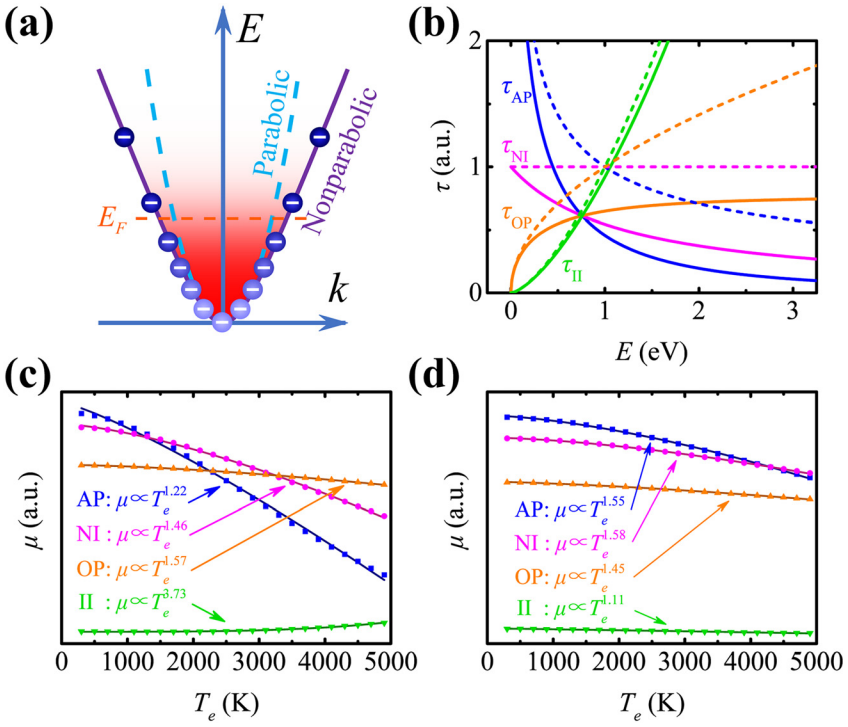

Figure 1: Simulation results. (a) Schematic diagram of electron distribution in a nonparabolic conduction band. The red color scale represents the distribution probability. (b) Electron energy–dependent scattering times of different mechanisms in parabolic (C = 0, dashed lines) and nonparabolic (C = 0.4191 eV^{-1}, solid lines) bands. Calculated T_e-dependent μ relations and the fitting power functions for different scattering mechanisms dominant in parabolic (c) and nonparabolic (d) bands. $N = 1.3 \times 10^{21}$cm^{-3} and $m_0^* = 0.2893\, m_e$ are used in the calculation.

until now is accepted as the dominant mechanism in ITO [19–21], has an increasing scattering time with increasing electron energy. If the ionized impurity scattering is always dominant, then the overall scattering time should get longer upon intraband pumping that elevates the electron population toward higher energy states. However, the experimental observation just shows the opposite, i.e., the scattering time decreases with the increase in pump power [7, 16]. Herein, the mobility-temperature relations are calculated as follows: $\mu = e\langle\tau\rangle/\langle m^*\rangle$, with varying T_e in Figure 1c for a parabolic band and in Figure 1d for a nonparabolic band and taking one scattering mechanism at a time in Eq. (3). A power law $\mu = \mu_0 + aT_e^b$ is derived under the nondegenerate electron assumption, and $b = s/2$ is derived for identifying the dominant scattering mechanism. Here, the fitting exponents describing the temperature dependence on mobility for degenerate electron in both parabolic and nonparabolic bands show that they do not agree with the often quoted typical values of −3/2 and 3/2 [1, 33] for acoustic phonon and ionized impurity scatterings, respectively. It should be noted that the value of τ_{0**} does not affect the value of exponents. These exponent indicators are derived by using the Boltzmann distribution for a nondegenerate semiconductor with parabolic bands, while ITO is a degenerate semiconductor for which the Fermi-Dirac distribution is applicable.

With $\langle\tau\rangle$ and $\langle m^*\rangle$ defined above, we may extend the Drude theory by expressing the plasma frequency ω_p and the damping factor γ (also called as the scattering frequency) as follows:

$$\omega_p^2 = \frac{Ne^2}{\varepsilon_0\langle m^*\rangle} \quad \text{and} \quad \gamma = \frac{1}{\langle\tau\rangle}, \tag{7}$$

where e is the electron charge and ε_0 is the vacuum permittivity. The relative permittivity in NIR wavelength range is given by the Drude model [13, 18].

$$\varepsilon_r(\omega) = \varepsilon_\infty - \frac{\omega_p^2}{\omega^2 + i\gamma\omega}, \tag{8}$$

where ε_∞ is the high-frequency permittivity and ω is the optical angular frequency. Hence, through optical measurement of transmittance and reflectance spectra, the scattering mechanisms can be confirmed.

A femtosecond-pump continuum-probe experimental setup (Figure 2a) is adopted to measure the transmittance (T) and reflectance (R) spectra (Figure 2b and c), from which the value of T_e and γ is extracted [7], with the femtosecond laser source operating at a wavelength of 1250 nm, a pulse width of 50 fs, and a repetition rate of 1 kHz. The pump beam is delayed and then focused on the sample at an incidence angle of 60°, with p-polarization to maximize the optical nonlinear response [6]. As the probe, a supercontinuum beam is generated by a sapphire in the

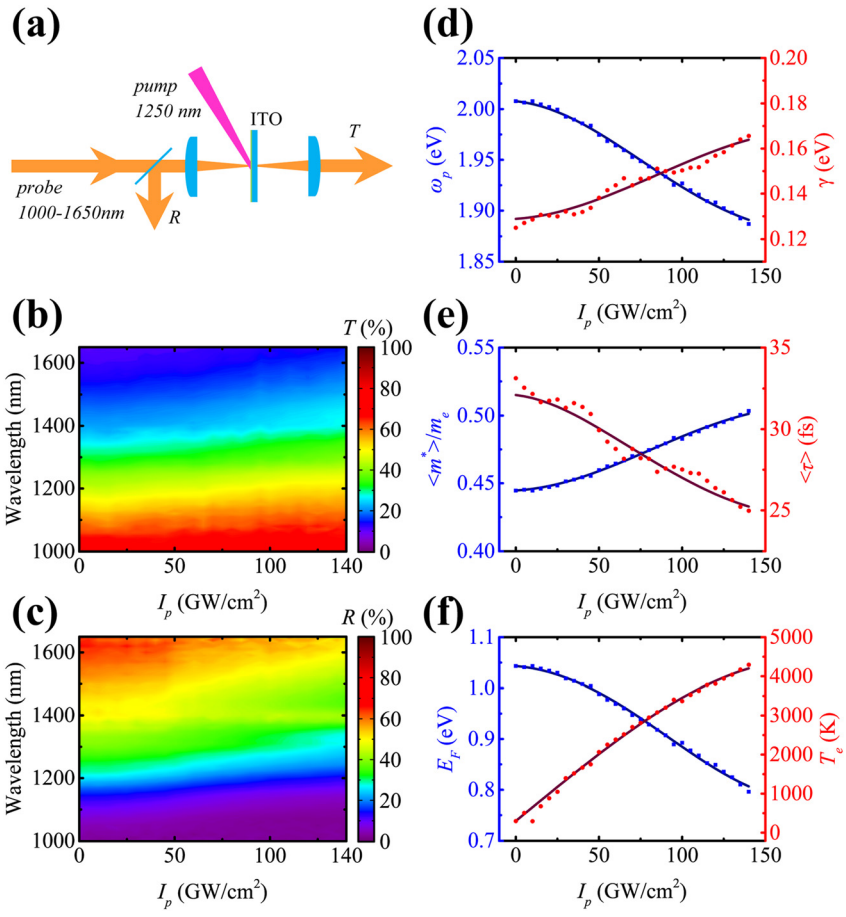

Figure 2: Experimental results. (a) Schematic of the femtosecond-pump continuum-probe experimental setup. Measured spectra of I_p-dependent transmittance T (b) and reflectance R (c). (d) Extracted I_p-dependent plasma frequency ω_p and damping factor γ (Eq. (7)). (e) Calculated electron overall effective mass $\langle m^*\rangle$ (Eq. (6)) and overall scattering time $\langle\tau\rangle$ (Eq. (4)). (f) Calculated Fermi level E_F and electron temperature T_e. The solid red lines of the $T_e \sim I_p$ relation in (f) is polynomial fitting, and the other solid lines in (d–f) are further calculated from the $E_F \sim T_e$ relation obtained from N conservation (Eqs. (5) and (7)) [7]. ITO: indium tin oxide.

spectral range of 1000–1650 nm, with a pulse width of 50 fs approximately, and then focused on the sample at normal incidence with a focal spot smaller than the pump spot. The intensity of the pump spot (I_p) is tuned in the range of 0–140 GW/cm^2, while the intensity of the probe spot is lower than 1 GW/cm^2 to avoid optical nonlinearity caused by the probe beam. The sample under test is a commercial ITO film (Supplier: Suzhou Research Materials Microtech Co., Ltd.) deposited on a 1.1-mm-thick flat optical glass substrate with a thickness of 220 nm and a Hall electron density of $N = 1.3 \times 10^{21}\,\mathrm{cm}^{-3}$. The first-order nonparabolicity factor of ITO is $C = 0.4191\,\mathrm{eV}^{-1}$ [14].

Both T and R spectra of the probe beam are measured for extracting ω_p and γ using Eq. (8), and then, electron parameters including $\langle m^*\rangle$, $\langle\tau\rangle$, E_F, and T_e are calculated (Eqs. (4)–(7)) [7]. $\varepsilon_\infty = 3.796$ and the ENZ wavelength at 1212 nm are obtained by fitting T and R spectra under zero pumping. The electron temperature herein is equal to the room temperature $T_e = 300\,\mathrm{K}$, and the calculation with $N = 1.3 \times 10^{21}\,\mathrm{cm}^{-3}$ deduces $m_0^* = 0.2893 m_e$, where m_e is the electron rest mass. The I_p-dependent T and R responses are measured at the delay with maximum change, and the dispersion in the experimental system induced supercontinuum probe chirp has been corrected (Figure 2b and c), and the corresponding Drude parameters (Figure 2d) and the electron parameters (Figure 2e and f) are then calculated using Eqs. (6) and (7) [7].

As shown in Figure 3a the experimentally derived $\gamma \sim T_e$ relation is fitted by using Eq. (4) with inclusion of the four scattering mechanisms, which provides four τ_{0**} factors and the corresponding 95% confidence bounds.

$$\begin{cases} \tau_{0\mathrm{AP}} = 0.087 & (0.084,\ 0.090) & \mathrm{ps\,eV^{1/2}} \\ \tau_{0\mathrm{NI}} = 1.3 \times 10^6 & (1.3 \times 10^6,\ 1.3 \times 10^6) & \mathrm{ps} \\ \tau_{0\mathrm{OP}} = 2.4 \times 10^7 & (2.4 \times 10^7,\ 2.4 \times 10^7) & \mathrm{ps\,eV^{-1/2}} \\ \tau_{0\mathrm{II}} = 0.39 & (0.36,\ 0.41) & \mathrm{ps\,eV^{-3/2}} \end{cases}. \quad (9)$$

The scattering time for the four scattering mechanisms calculated from the above results and Eq. (4) is shown in Figure 3a. The acoustic phonon scattering and ionized impurity scattering can be easily identified as the two most significant mechanisms because of their short scattering time, while neutral impurity scattering and optical phonon scattering can be identified as negligible mechanisms because of their extremely long scattering time (>10^6 fs). We also implemented the fitting with a model containing only

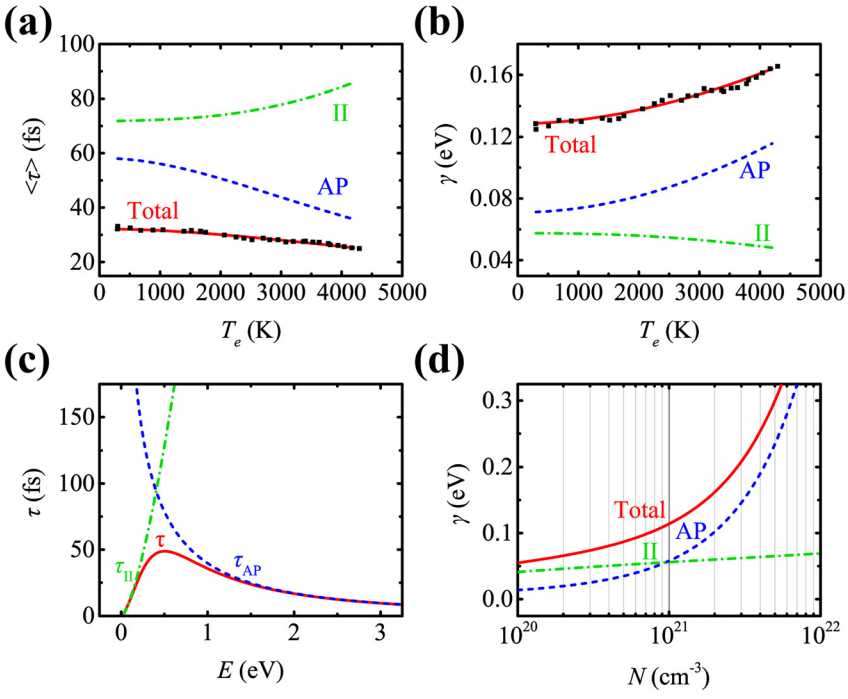

Figure 3: (a) Fitted $\langle\tau\rangle \sim T_e$ relation and scattering time for acoustic phonon (AP) scattering and ionized impurity (II) scattering. (b) Calculated $\gamma \sim T_e$ relation and contribution for acoustic phonon (AP) scattering and ionized impurity (II) scattering. (c) Electron energy–dependent scattering time $\tau(E)$, $\tau_{AP}(E)$, and $\tau_{II}(E)$. (d) Electron density N dependent damping factor γ at T_e = 300 K with the contribution for AP and II scattering.

acoustic phonon scattering and ionized impurity scattering; the results and the corresponding 95% confidence bounds are almost unchanged. The very high values of τ_{0NI} and τ_{0OP} are inaccurate and not representative. The total γ shown in Figure 3b is calculated by Eq. (7), and the contributions of each scattering mechanism are calculated by taking one scattering mechanism at a time in Eq. (3). The contributions of acoustic phonon scattering and ionized impurity scattering show opposite T_e dependence, with the former increasing with the increase in T_e, i.e., via optical pumping. Figure 3c indicates that acoustic phonon scattering and ionized impurity scattering are more influential on high- and low-energy electrons, respectively. This explains the trends well that the acoustic phonon scattering is more significant under high T_e (shorter scattering time), as shown in Figure 3a, because electrons are pumped to higher energy states. This can be easily understood from the fact that the interaction of an electron with ionized impurity is more effective at low electron velocity (low T_e) as it spends longer time in the vicinity of the ionized impurity than at high velocity. At high velocity, the electron is more likely to collide with lattice atoms, and thus, phonon scattering is more probable at high electron velocity [37, 38].

The acoustic phonon scattering shown in Figure 3a is not always dominant because the electron density dependence needs to be examined. We correct τ_{0AP} and τ_{0II} for varying N according to their detailed form $\tau_{0AP} \propto (m^*)^{3/2}$ [39] and $\tau_{0II} \propto \sqrt{m^*}/N_I$ [34], where N_I is the ionized impurity concentration and $N_I \propto N$ because ionized impurity acts as the donor of free carriers. As shown by simulation for zero pumping, the contributions of acoustic phonon scattering and ionized impurity scattering vary with N (Figure 3d) and are equal at $N_c = 0.95 \times 10^{21}$ cm^{-3}. The results shown in Figure 3d indicate the N-dependency of γ; however, such prediction should be carefully used as there may be more physical mechanisms beyond the model that affect scattering.

In summary, multiple electron scattering mechanisms are investigated by taking into account hot electron distribution in the nonparabolic conduction band, and the damping factor of the extended Drude model for describing ENZ optical nonlinearity is obtained. We show that the exponent rule of the mobility-temperature relation cannot be applied to infer the dominant scattering mechanism in ITO owing to high electron density and consequently the Fermi-Dirac distribution. Through the femtosecond-pump continuum-probe experiment on ITO, acoustic phonon scattering and ionized impurity scattering are identified as the two major scattering mechanisms, which play a more important role for high-energy and low-energy electrons, respectively. By heating up the electrons, such as by external intraband optical pumping at ENZ wavelength, the influence of acoustic phonon scattering is increased, while that of ionized impurity scattering is reduced. As the total electron density is increased, there exists a critical electron density at 0.95×10^{21} cm^{-3}, whereby acoustic phonon scattering crosses over to ionized impurity scattering and the damping factor varies with electron density.

With knowledge of electron dynamics, a complete model of ENZ optical nonlinearity can be further accomplished.

Acknowledgments: We acknowledge the financial support from the Natural Science Foundation of China (NSFC) (grant no. 91950207, no. 61675171, and no. 61675169).

References

[1] H. Hosono, D. C. Paine, and D. Ginley, *Handbook of Transparent Conductors*, New York, USA, Springer Science & Business Media, 2010.
[2] J. Gao, K. Kempa, M. Giersig, E. M. Akinoglu, B. Han, and R. Li, "Physics of transparent conductors," *Adv. Phys.*, vol. 65, pp. 553–617, 2016.
[3] N. Xinxiang, H. Xiaoyong, C. Saisai, and G. Qihuang, "Epsilon-near-zero photonics: a new platform for integrated devices," *Adv. Opt. Mater.*, vol. 6, p. 1701292, 2018.
[4] N. Kinsey, C. DeVault, A. Boltasseva, and V. M. Shalaev, "Near-zero-index materials for photonics," *Nat. Rev. Mater.*, vol. 4, pp. 742–760, 2019.
[5] O. Reshef, I. De Leon, M. Z. Alam, and R. W. Boyd, "Nonlinear optical effects in epsilon-near-zero media," *Nat. Rev. Mater.*, vol. 4, pp. 535–551, 2019.
[6] M. Z. Alam, I. De Leon, and R. W. Boyd, "Large optical nonlinearity of indium tin oxide in its epsilon-near-zero region," *Science*, vol. 352, pp. 795–797, 2016.
[7] H. Wang, K. Du, C. Jiang, et al., "Extended Drude model for intraband-transition-induced optical nonlinearity," *Phys. Rev. Appl.*, vol. 11, p. 064062, 2019.
[8] V. Krasavin Alexey, P. Ginzburg, and V. Zayats Anatoly, "Free-electron optical nonlinearities in plasmonic nanostructures: a review of the hydrodynamic description," *Laser Photon. Rev.*, vol. 12, p. 1700082, 2017.
[9] P. Guo, R. D. Schaller, J. B. Ketterson, and R. P. Chang, "Ultrafast switching of tunable infrared plasmons in indium tin oxide nanorod arrays with large absolute amplitude," *Nat. Photon.*, vol. 10, pp. 267–273, 2016.
[10] I. Hamberg, and C. G. Granqvist, "Optical properties of transparent and heat-reflecting indium tin oxide films: refinements of a model for ionized impurity scattering," *J. Appl. Phys.*, vol. 59, pp. 2950–2952, 1986.
[11] R. Bel Hadj Tahar, T. Ban, Y. Ohya, and Y. Takahashi, "Tin doped indium oxide thin films: electrical properties," *J. Appl. Phys.*, vol. 83, pp. 2631–2645, 1998.
[12] Z. Ma, Z. Li, K. Liu, C. Ye, and V. J. Sorger, "Indium-tin-oxide for high-performance electro-optic modulation," *Nanophotonics*, vol. 4, pp. 198–213, 2015.
[13] M. D. Losego, A. Y. Efremenko, C. L. Rhodes, M. G. Cerruti, S. Franzen, and J.-P. Maria, "Conductive oxide thin films: model systems for understanding and controlling surface plasmon resonance," *J. Appl. Phys.*, vol. 106, p. 024903, 2009.
[14] X. Liu, J. Park, J.-H. Kang, et al., "Quantification and impact of nonparabolicity of the conduction band of indium tin oxide on its plasmonic properties," *Appl. Phys. Lett.*, vol. 105, p. 181117, 2014.
[15] B. T. Diroll, P. Guo, R. P. H. Chang, and R. D. Schaller, "Large transient optical modulation of epsilon-near-zero colloidal nanocrystals," *ACS Nano*, vol. 10, pp. 10099–10105, 2016.
[16] J. Kim, E. G. Carnemolla, C. DeVault, et al., "Dynamic control of nanocavities with tunable metal oxides," *Nano Lett.*, vol. 18, pp. 740–746, 2018.
[17] G. V. Naik, J. Kim, and A. Boltasseva, "Oxides and nitrides as alternative plasmonic materials in the optical range [Invited]," *Opt. Mater. Express*, vol. 1, pp. 1090–1099, 2011.
[18] G. V. Naik, V. M. Shalaev, and A. Boltasseva, "Alternative plasmonic materials: beyond gold and silver," *Adv. Mater.*, vol. 25, pp. 3264–3294, 2013.
[19] G. Frank, and H. Köstlin, "Electrical properties and defect model of tin-doped indium oxide layers," *Appl. Phys. A*, vol. 27, pp. 197–206, 1982.
[20] R. Bel Hadj Tahar, T. Ban, Y. Ohya, and Y. Takahashi, "Electronic transport in tin-doped indium oxide thin films prepared by sol-gel technique," *J. Appl. Phys.*, vol. 83, pp. 2139–2141, 1998.
[21] H. Kim, C. Gilmore, A. Pique, et al., "Electrical, optical, and structural properties of indium–tin–oxide thin films for organic light-emitting devices," *J. Appl. Phys.*, vol. 86, pp. 6451–6461, 1999.
[22] I. Hamberg, and C. G. Granqvist, "Optical properties of transparent and heat-reflecting indium tin oxide films: the role of ionized impurity scattering," *Appl. Phys. Lett.*, vol. 44, pp. 721–723, 1984.
[23] I. Hamberg, and C. G. Granqvist, "Evaporated Sn-doped In2O3 films: basic optical properties and applications to energy-efficient windows," *J. Appl. Phys.*, vol. 60, pp. R123–R160, 1986.
[24] R. J. Mendelsberg, G. Garcia, and D. J. Milliron, "Extracting reliable electronic properties from transmission spectra of indium tin oxide thin films and nanocrystal films by careful application of the Drude theory," *J. Appl. Phys.*, vol. 111, p. 063515, 2012.
[25] C. Guillén, and J. Herrero, "Structure, optical, and electrical properties of indium tin oxide thin films prepared by sputtering at room temperature and annealed in air or nitrogen," *J. Appl. Phys.*, vol. 101, p. 073514, 2007.
[26] Y. Wang, A. Capretti, and L. Dal Negro, "Wide tuning of the optical and structural properties of alternative plasmonic materials," *Opt. Mater. Express*, vol. 5, p. 2415, 2015.
[27] W. Heng, D. Xinhai, D. Kang, et al., "Tuning epsilon-near-zero wavelength of indium tin oxide film via annealing," *J. Phys. Appl. Phys.*, vol. 53, p. 225108, 2020.
[28] C. K. Sun, F. Vallée, L. Acioli, E. P. Ippen, and J. G. Fujimoto, "Femtosecond investigation of electron thermalization in gold," *Phys. Rev. B*, vol. 48, pp. 12365–12368, 1993.
[29] R. H. M. Groeneveld, R. Sprik, and A. Lagendijk, "Femtosecond spectroscopy of electron–electron and electron–phonon energy relaxation in Ag and Au," *Phys. Rev. B*, vol. 51, pp. 11433–11445, 1995.
[30] N. Del Fatti, C. Voisin, M. Achermann, S. Tzortzakis, D. Christofilos, and F. Vallée, "Nonequilibrium electron dynamics in noble metals," *Phys. Rev. B*, vol. 61, pp. 16956–16966, 2000.
[31] C. Chen, Z. Tao, A. Carr, et al., "Distinguishing attosecond electron–electron scattering and screening in transition metals," *Proc. Natl. Acad. Sci. USA*, vol. 114, pp. E5300–E5307, 2017.

[32] J. Kolodziejczak, and S. Zukotyński, "Galvano-and thermomagnetic effects in semiconductors with non-spherical and non-parabolic energy bands," *Phys. Status Solidi*, vol. 5, pp. 145–158, 1964.
[33] Y. Peter, and M. Cardona, *Fundamentals of Semiconductors: Physics and Materials Properties*, Berlin, Springer Science & Business Media, 2010.
[34] D. Chattopadhyay, and H. J. Queisser, "Electron scattering by ionized impurities in semiconductors," *Rev. Mod. Phys.*, vol. 53, pp. 745–768, 1981.
[35] B. K. Ridley, *Quantum Processes in Semiconductors*, Oxford, Oxford University Press, 2013.
[36] J. Singh, *Electronic and Optoelectronic Properties of Semiconductor Structures*, Cambridge, Cambridge University Press, 2007.
[37] B. M. Askerov, *Electron Transport Phenomena in Semiconductors*, Singapore, World Scientific, 1994.
[38] M. Lundstrom, *Fundamentals of Carrier Transport*, Cambridge, Cambridge University Press, 2009.
[39] S. S. Li, *Semiconductor Physical Electronics*, Berlin, Springer Science & Business Media, 2012.